IGC Newsletter

ISSN 0972-5741 Volume 138, Issue 4, October 2023

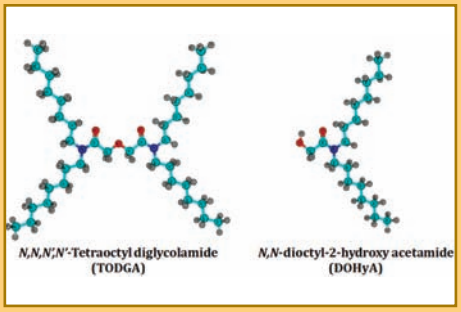

Director's Message

Dear Colleagues,

FBTR completed the 32nd irradiation campaign on 8.09.2023 at the design target power of 40 MWt/10MWe. The total electrical energy generated in this campaign is 19.5 MU. IGCAR organised Anu Awareness Yatra – 2023 with the theme 'ATOMS IN THE SERVICE OF THE NATION' in association with the National Council of Science Museum (NCSM), Ministry of Culture, Government of India, Vigyan Bharathi – Arivial Sangam, Tamil Nadu, and Indian Association for Radiation Protection. The programmes were organised in nodal institutions in seven districts in Tamil Nadu and three in Kerala as part of Azadi Ka Amrit Mahotsav, and to showcase the indigenous progress in science and technology. The Yatra started at Kalpakkam and culminated at IREL (India) Limited, Aluva travelling more than 1000 kms, covering Kancheepuram, Thiruvannamalai, Salem, Erode, Karur, Coimbatore, Palakkad, Thrissur and Kochi.

The 31st Prof. Brahm Prakash Memorial Materials Quiz (BPMMQ) was organized by the Indian Institute of Metals- Kalpakkam Chapter and IGCAR in Kalpakkam during September 8-9, 2023, drawing participation of 80 students from various schools across India. Prof. B. S. Murty, Director, IIT Hyderabad delivered the Prof Brahm Prakash Memorial lecture on 'The immeasurable joy of research'. IGCAR has been provisionally selected this year for a grant of Atal Incubation Centre (AIC).

I appreciate the efforts of the editorial committee and the authors for their contributions to the newsletter

[B. Venkatraman]
Director, IGCAR & GSO

Editor's Desk

Dear Reader

Greetings

It is my pleasant privilege to forward the latest issue of IGC Newsletter (Volume 138, October 2023, Issue 4). I thank my team for their timely inputs, cooperation, and support in bringing out this issue.

The technical article of this issue "Effect of Enrichment on the Thermal Expansion of Boron Carbide" is by Dr. Haraprasanna Tripathy and colleagues from PMD, MMG, MCMFG, IGCAR.

Young Officer's Forum features an article on "Preparation of 316L(N) stainless steel weld joints containing 0.05 to 0.14 wt.% N and study on its microstructure and properties" by Dr. Namrata Upadhyay from MMG, IGCAR.

The article on "Electrochemical Noise an Online Corrosion Monitoring tool to evaluate Localized Corrosion in Stainless Steel " by Shri S. Kumar from SQRMG, IGCAR is categorised as this issue's Young Researcher article.

In the back cover, we have Lesser Goldenback bird very commonly found in both IGCAR campus and Kalpakkam township.

The Editorial Committee would like to thank all the contributors. We look forward to receiving constructive suggestions from readers towards improving the IGC Newsletter content.

We express our deepest gratitude to Director IGCAR for his keen interest and guidance.

With best wishes and regards

S. Rajeswari
Chairman, Editorial Committee, IGC Newsletter and
Head, Scientific Information Resource Division, IGCAR

Effect of Enrichment on the Thermal Expansion of Boron Carbide

Boron carbide (B_4C) is one of the most important solids used for several nuclear applications all over the world, owing to its excellent neutron absorption cross section. The neutron absorption capability of boron carbide depends on its ^{10}B isotope content as the absorption cross section of ^{10}B (3837 b) is significantly higher than the principal isotope ^{11}B (0.005 b). For a fast neutron spectrum, adequate ^{10}B enrichment is necessary for boron carbide to be used as an effective neutron absorber as the absorption cross section decreases with increase in neutron energy. The extent of enrichment depends on the specific application either for emergency shutdown or power control systems, neutron shielding or neutron detectors etc.

As a part of the core modification programme to attain the design power output of 40 MWt, 50 % ^{10}B enriched B_4C (50E-B_4C) has been recently introduced as a burnable poison in Fast Breeder Test reactor (FBTR). The absorber rods in FBTR uses B_4C with 90% ^{10}B enrichment (90E-B_4C) and B_4C with natural ^{10}B isotopic composition (N-B_4C) is used for the neutron shielding applications. As the two isotopes ^{10}B and ^{11}B in boron carbide differ in mass by ~10%, the coefficient of thermal expansion (CTE) is anticipated to undergo significant change due to ^{10}B enrichment. However B_4C is believed to have a complex and highly distorted structure with random distribution of carbon atoms among the lattice sites which makes it difficult to accurately predict the thermodynamic properties. In addition to this, when isotopic effect is considered, the occupation of one B site by either ^{10}B or ^{11}B further complicates the structure and properties. The lattice thermal expansion (LTE) of B_4C measured from diffraction methods can possibly differ from the bulk thermal expansion (BTE) measured from dilatometry due to the presence of intrinsic defects and disorder. In this regard, the present study is focused towards the experimental measurement and comparison of LTE and BTE of N-B_4C, 50E-B_4C and 90E-B_4C in order to address the effect of ^{10}B enrichment as well as the role of defects on the thermal expansion behavior of B_4C.

The crystal structure of boron carbide (shown in Figure 1) consists of a 12 atom icosahedra (B_{12} or $B_{11}C$) located at the vortices of a rhombohedral Bravais lattice (space group- $R\bar{3}m$) and a three atom linear chain consisting of either CBC or CBB or B□B element (□, vacancy) along the main diagonal of the rhombohedra. This structure is also described based on a non primitive hexagonal unit cell where the [111] rhombohedral axis matches with the [0001] hexagonal axis. The rhombohedral and hexagonal unit cell of B_4C is shown in Figure 1a and 1b respectively.

Hot pressed B_4C pellets with natural as well as 50% and 90% enriched ^{10}B composition were received from Heavy Water Board, Manuguru, India. Chemical and isotopic composition of the boron carbide specimens containing natural and enriched ^{10}B were carried out using wet chemical analysis as well as inductively coupled plasma mass spectrometry (ICPMS) and the results are given in Table 1.

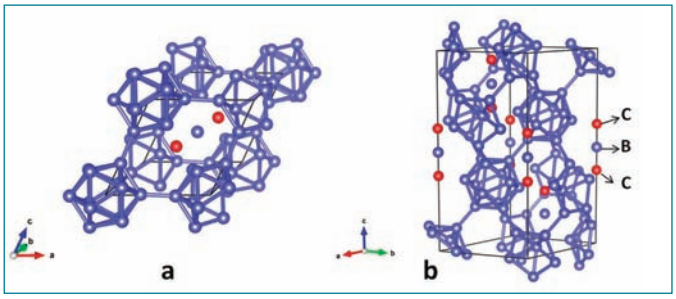

Fig. 1: Atomic structure of boron carbide (a) Rhombohedral (b) Hexagonal unit cell

The measured density of hot pressed N-B_4C, 50E-B_4C and 90E-B_4C pellets were found to be 2.449, 2.423 and 2.326 gcc^{-1} respectively with a measurement uncertainty of $\pm$ $1x10^{-4}$ gcc^{-1}. Back scattered electron (BSE) imaging, X-ray elemental mapping and quantitative micro-chemical analysis of N-B_4C, 50E-B_4C and 90E-B_4C pellets were carried out using electron probe micro analyzer (EPMA). Figure 2a shows the BSE image of N-B_4C pellet and the corresponding X-ray elemental maps obtained for boron and carbon are shown in Figure 2b and c respectively. Representative BSE images and X-ray maps for boron and carbon are shown in Figures 2(d-f) for 50E-B_4C and Figure 2(g-i) for 90E-B_4C. The BSE images indicate the presence of graphite particles (agglomerates and secondary

Table 1 Chemical and isotopic composition of natural and enriched B_4C

Element	N-B_4C	50E-B_4C	90E-B_4C
10B (atom %)	19.90±0.3	52.93±0.04	94.5±0.01
Boron (wt. %)	81.0	77.6±0.78	76.4±0.76
HNO_3 soluble boron	< 0.5%	0.04 %	1.0 %
Water soluble boron	< 0.2%	0.014 %	0.25 %
Fluoride	< 25 μg/g	< 20 μg/g	< 20 μg/g
chloride	<75 μg/g	< 50 μg/g	< 50 μg/g
other impurities	Ca<0.3% Fe<1.0%	W ~ 1.03 % Ca < 400 ppm Ni < 0.04 % Fe ~750 ppm	W ~ 0.1% Ca < 0.04% Ni ~ 700 ppm Fe 1140-1260 ppm
Total Boron + Total Carbon	98.0 %	98.8%	96.61 %
Carbon	20.3±0.2%	21.2±0.2 %	19.1± 1.0 %

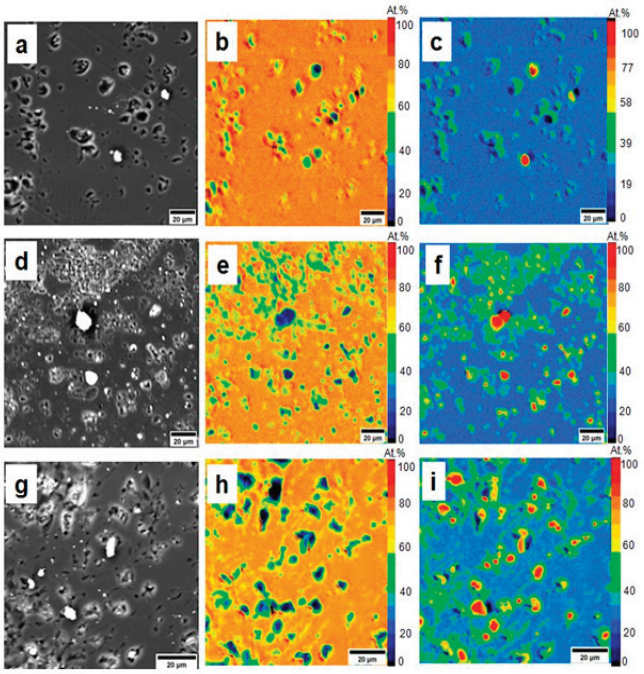

Fig. 2: BSE image and X-ray elemental maps obtained for boron and carbon for N-B4C ((a)-(c)), 50E-B4C ((d)-(f)) and 90E-B4C ((g)-(i)) respectively

particles) in accordance with the equilibrium phase diagram prediction where a mixture of B_4C+ graphite is anticipated for a carbon composition beyond carbon rich limit of the homogeneity range. The distribution of graphite particles was found to be non-uniform in the microstructure.

1. Lattice Thermal Expansion (LTE):

The high temperature X-ray diffraction profiles (298-1273 K at each 100 K interval) is shown in Figures 3a, b and c for N-B_4C, 50E-B_4C and 90E-B_4C respectively at select temperatures. The rhombohedral B_4C phase is observed in all the specimens though additional peak corresponding to carbon could be seen only in N-B_4C which can be attributed to the inhomogeneous distribution of these second phase particles. The diffraction peaks were analyzed and the lattice parameters for the hexagonal cell were measured for N-B_4C (a = 5.595 A0, c = 12.070 A0), 50E-B_4C (a = 5.615 A0, c = 12.095 A0) and 90E-B_4C (a = 5.617 A0, c = 12.099 A0) at room temperature. The temperature dependence of lattice parameters along -a and -c axis (a_(T) and c_T)

is plotted in Figures 4a and b and subjected to nonlinear regression analysis using the following empirical expression to obtain linear thermal expansion of the hexagonal unit cell.

$$a_T\left(A^0\right) = a_0 + a_1(T-298) + a_2(T-298)^2 \quad (1)$$

$$c_T\left(A^0\right) = c_0 + c_1(T-298) + c_2(T-298)^2 \quad (2)$$

In the above expression, T stands for temperature in K and the parameters, a_0, a_1, a_2 and c_0, c_1, c_2 are fit constants determined from the non linear fitting of the measured values. The % expansion (ε_a) and mean coefficients of linear thermal expansion for the -a axis (α_a^{mean})can be determined using the following expressions

$$\varepsilon_a = \frac{a_T - a_{298}}{a_{298}} \times 100 \quad (3)$$

$$\alpha_a^{mean} = \frac{1}{a_{298}} \frac{(a_T - a_{298})}{(T-298)} \quad (4)$$

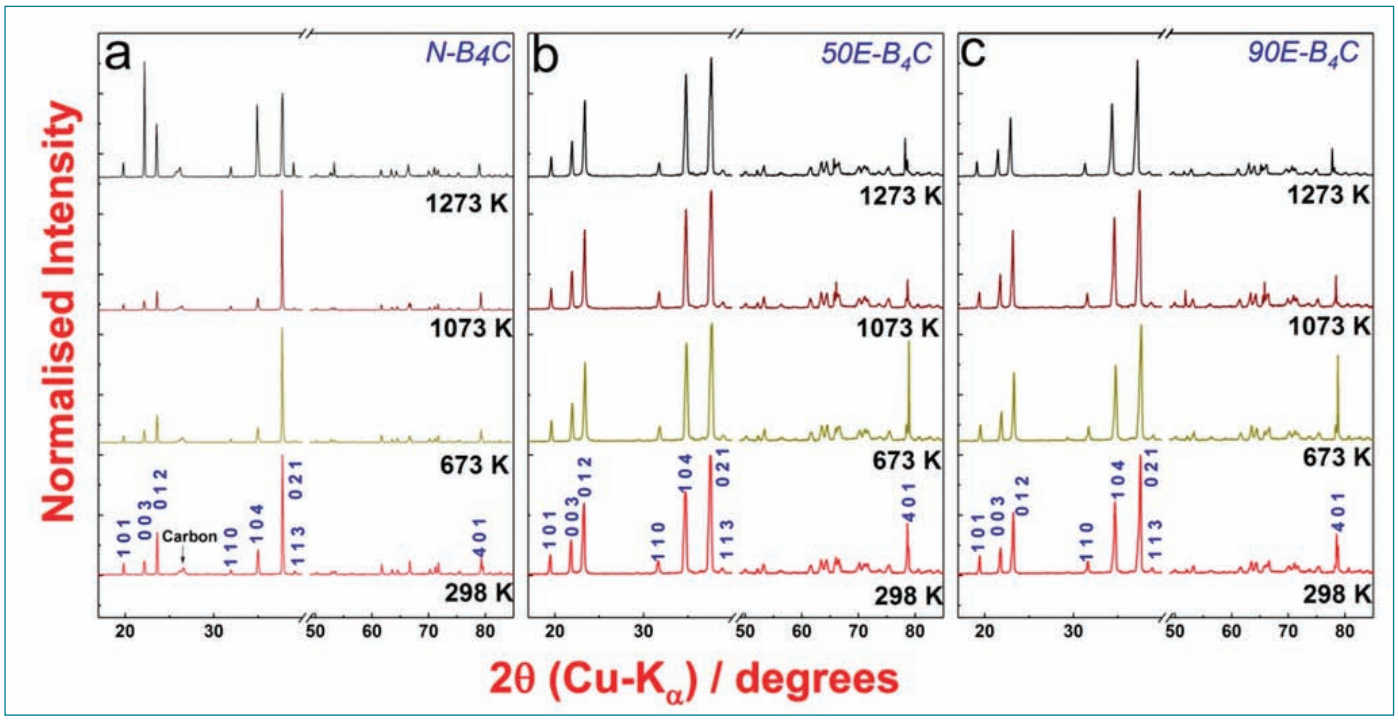

Fig. 3: High temperature XRD patterns for (a) N-B_4C (b) 50E-B_4C and (c) 90E-B_4C

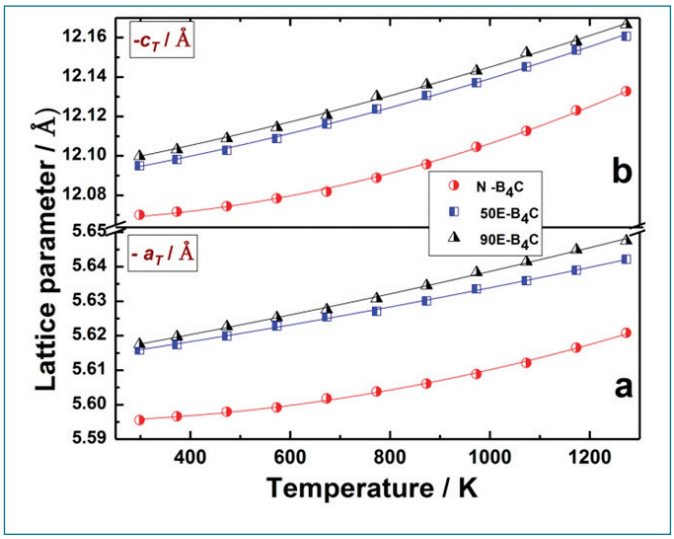

Fig. 4: Lattice parameters (scattered points) for N-B_4C, 50E-B_4C and 90E-B_4C and the non linear regression fitting (solid lines)

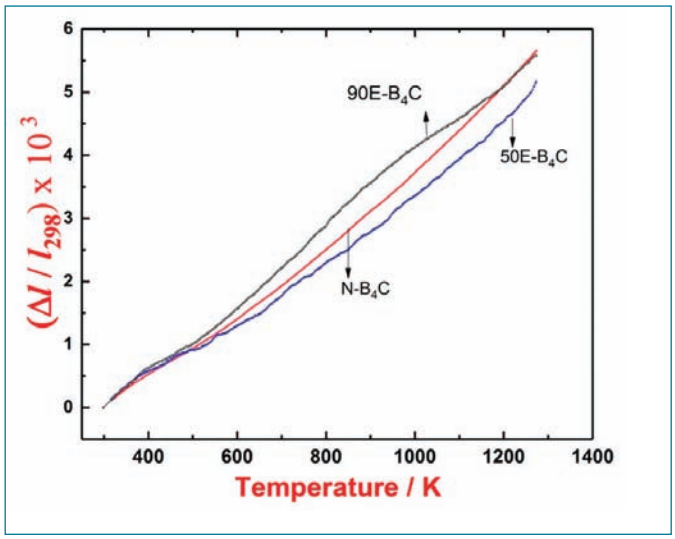

Fig. 5: Dilatational strain measured as a function of temperature for N-B4C and enriched B4C

The linear expansion for the -c axis (ε_c, (α_a^{mean})) were found out in a similar manner using fit parameters c_0, c_1 and c_2. For polycrystalline B_4C specimens, average value of linear coefficient of thermal expansion (α_l^{avg}), is obtained using

$$\alpha_l^{avg} = \frac{2\alpha_a^{mean} + \alpha_c^{mean}}{3} \qquad (5)$$

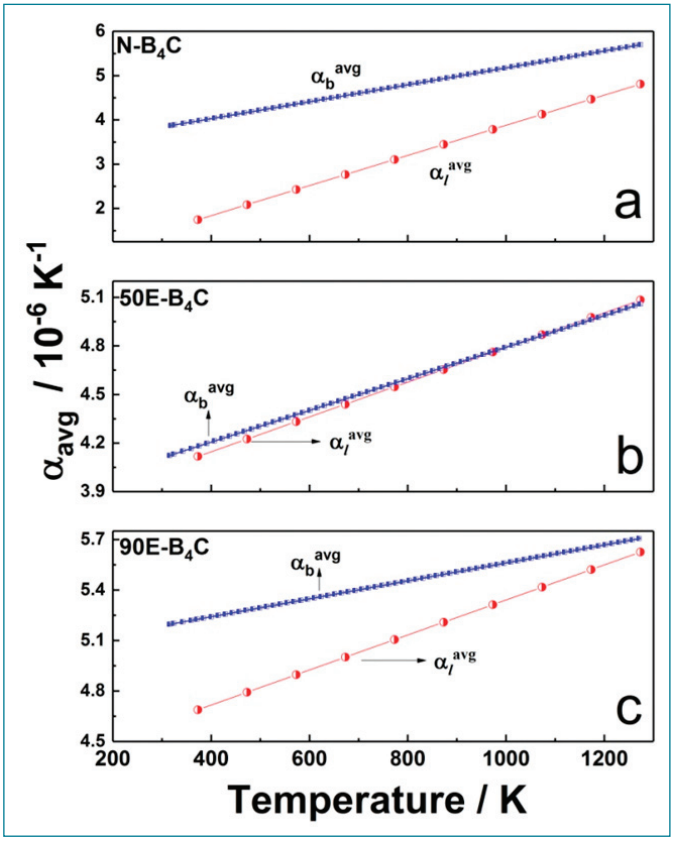

Fig. 56: Comparison of LTE ($\alpha_l$avg) measured from XRD with that of the BTE $\alpha_b^{avg}(=\alpha_b^{mean})$ measured from the dilatometry for N-B4C, 50E-B4C , 90E-B4C

2. Bulk Thermal Expansion (BTE):

The dilatational strain $(\Delta l/l_{298})$ measured using push rod dilatometer as a function of temperature for natural and enriched B_4C specimens are shown in Figure 5, where Δl represents the temperature induced dilatation and l_{298} stands for the length at room temperature for the polycrystalline B_4C specimen. For the estimation of BTE, the measured length of the specimens $(l_{298}+\Delta l)$ was subjected to non linear regression analysis using a second order polynomial.

$$l_T(\mu m) = l_0 + l_1(T-298) + l_2(T-298)^2 \qquad (6)$$

The fit parameters l_0, l_1 *and* l_2 were evaluated from the least square fitting of the experimental data. The bulk linear thermal expansion coefficients i.e εb, (α_a^{mean}) was evaluated using equations (3)-(4) where aT and a_{298} are replaced by l_T and l_{298}. The average value of the bulk linear expansion i.e $\alpha_b^{avg}(=\alpha_b^{mean})$ estimated from the dilatometry results is the directionally averaged expansion along the -a and -c axial directions for polycrystalline B_4C.

Figures 6a-c depict the variation of the average value of BTE α_b^{avg} estimated from the dilatometry in comparison with the LTE estimated from lattice parameter variation (α_l^{avg}) for natural and enriched B_4C. The results show that, (i) the average CTE increases with increase in ^{10}B enrichment for polycrystalline B_4C (ii) bulk expansion is always higher compared to the lattice expansion (iii) the difference in bulk and lattice expansion is minimum for 50E-B_4C whereas it is significant for N-B_4C and 90E- B_4C and (iv) the difference in bulk and lattice expansion gradually comes down with increase in temperature i.e. there is a strong temperature dependence of lattice expansion compared to the bulk expansion irrespective of the ^{10}B content.

The lattice parameter at a finite temperature solely depends on the atomic radii, the nature of chemical bonding as well as the effect of zero point displacement which purely originates from the quantum nature of matter. The substitution of one isotope with another in a solid doesn't affect the bonding characteristics and have no significant effect on the structure of the potential energy. Therefore the change in lattice parameter due to isotopic substitution is attributed solely to the zero point displacement and the temperature induced volume expansion. With increase in the relative mass difference between the isotopes, the vibrational and rotational frequencies of molecules are expected to increase; which can cause a change in the lattice parameter and in the coefficient of thermal expansion. The concentration of CBC, CBB and B□B units in the B_4C unit cell depends on its carbon composition. These individual units with different sizes and electric charges are responsible for generation of high defect concentrations in the material. The carbon atom in the B11C icosahedra can possibly substitute the B atoms at six different polar sites and the boron atoms can possibly replace the C atoms at the end of CBC chain. This suggests that the elementary cell that represents the compound is not unique unlike the case for an ideal crystal. In addition to this, when isotopic effect is considered, the occupation of one B site by either ^{10}B or ^{11}B further increases the number of possible elementary cells. This structural complexity is expected to be maximum at 50% enrichment which is possibly reflected in the measured bulk dilatational strain shown in Figure 5, where $\Delta l/l_{298}$ for 50E-B_4C is found to be lower compared to N-B_4C and 90E-B_4C above 600 K.

While X-ray method provides information on the temperature dependence of unit cell expansion of a crystalline solid, dilatometry is used for the bulk expansion measurements irrespective of the crystal structure of the solid. In the case of alloys and stoichiometric compounds, thermal expansion coefficients are generally affected by the presence of defects at very high temperatures. The evidence for this fact can be also observed from Figure 5, where the difference in $\Delta l/l_{298}$ is negligible below 600 K but increases with increase in temperature.

In the present study, significant difference is observed between the lattice and bulk expansion for N-B_4C and 90E-B_4C although this difference is small for 50E-B_4C. This can possibly be explained based on the presence of defects in the specimen which is manifested as a difference in density. It is always difficult to achieve theoretical density for boron carbide due to the presence of strong covalent bonds. The lower density which is generally attributed to the presence of defects such as voids and pores in the specimens are introduced during the process of sintering. In the measurement of bulk expansion, these three dimensional (3D) defects are also subjected to thermally induced dilation and hence contribute towards total expansion. On the other hand, the lattice parameter measured from X-ray diffraction only indicates the expansion in the unit cell which is unperturbed by the processing induced defects. This is the primary reason behind the observed difference between the lattice and bulk expansion in boron carbide at low temperatures. In the present investigation, the relative density of 50E-B_4C is maximum (99.1%) in comparison to 90E-B_4C (98.1%) and N-B_4C (97.2%). This difference is manifested in the observed temperature dependence of the bulk and lattice thermal expansion coefficients.

The 50E-B_4C specimen with density close to the theoretical density shows only a minor difference between the bulk and lattice thermal expansion. In essence the significant difference in the lattice and bulk expansion coefficient in boron carbide is attributed to the density deficit in the material due to the presence of defects and impurities. Although the lattice expansion is vital in understanding the vibrational thermodynamic aspects of the system, for all practical purposes the bulk expansion coefficients play the crucial role for the design and development of engineering components for nuclear applications.

Reported by
Dr. Haraprasanna Tripathy
PMD, MMG

Young Officer's Forum

Dr. Namrata Upadhyay did her M.Sc in Chemistry from Banaras Hindu University in 2008. She joined the Corrosion Science and Technology Division, IGCAR in the year 2012 as Technical Officer C. Presently, she is working as Technical Officer-E. Her research interests are electrochemical techniques, corrosion testing and monitoring and electrochemical noise studies on nuclear materials.

Electrochemical Noise an Online Corrosion Monitoring tool to evaluate Localized Corrosion in Stainless Steel

1. Electrochemical Noise

Electrochemical noise (EN) measurement technique is commonly used to detect and monitor corrosion processes on stainless steel (SS). EN measurement involves the continuous monitoring of the electric potential and current signal in an electrolytic cell, which is typically composed of the SS samples and a reference electrode. The resulting data, known as electrochemical noise spectra, can be analyzed to extract information about the corrosion processes occurring on the SS surface. One of the main advantages of EN is its ability to detect and monitor localized corrosion, which is a common type of corrosion that occurs on SS. EN analysis finds advantage over the conventional method as it can identify metal corrosion at the equilibrium Open Circuit Potential (EOCP) without any external potential disruption and can be used for on-field applications.

The studies attempts to elucidate EN method for assessing SS's IGC and pitting susceptibility.

2. Electrochemical Noise Studies to Monitor Intergranular Corrosion in Austenitic SS

EN technique was used to study IGC in the sensitized AISI Type 316LN SS. The specimens underwent sensitization at temperatures

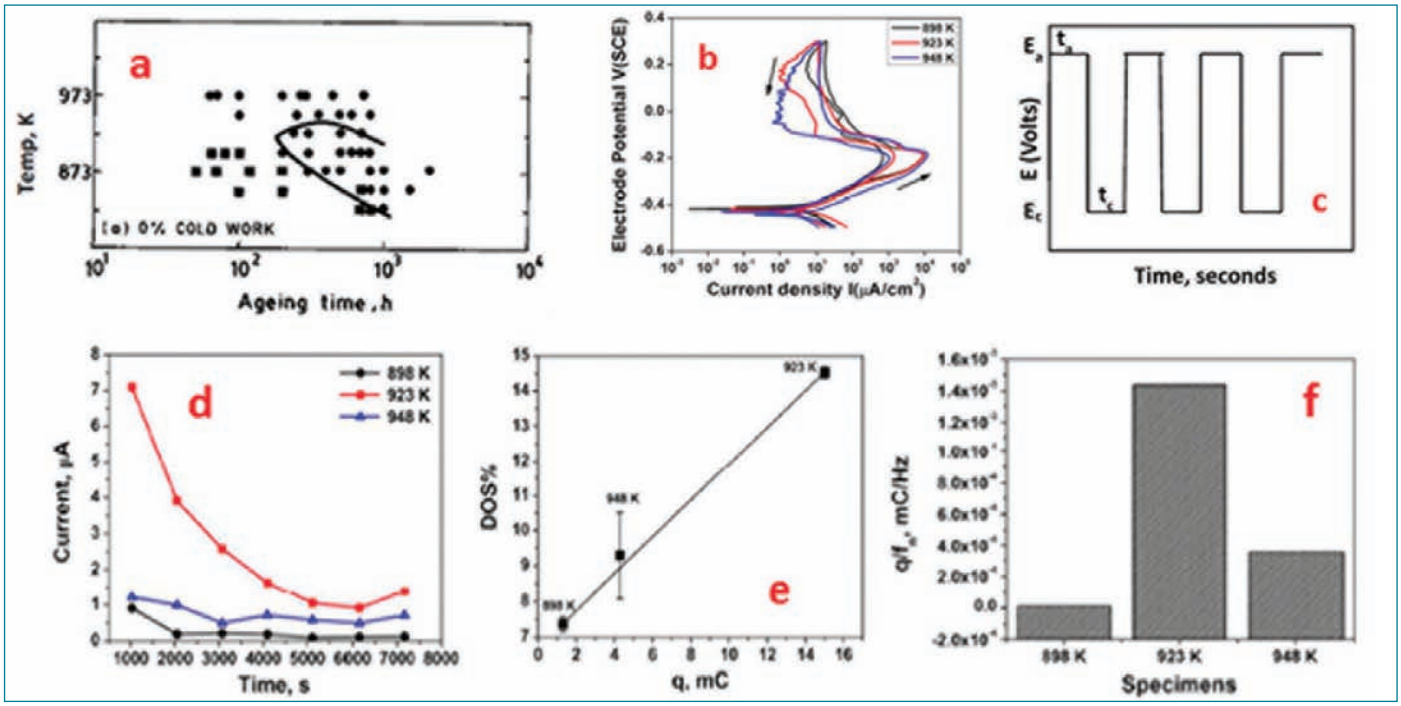

Fig. 1: TTS diagram for 316LN SS (a), DLEPR curve for 316LN SS sensitized at 898, 923 and 948 K for 500 h in 0.5 M H2SO4 + 0.01 M ammonium thiocyanate solution (b), Schematic of pulse polarization at 0.2 and -0.191 V each for 5 s (c), Plot of σI values as a function of time after EN measurements for 2 h (d), correlation between the DOS values from DLEPR and the charge (mC) value from EN analysis (e), Plot showing q/fn value for the sensitized specimens of 316LN SS.

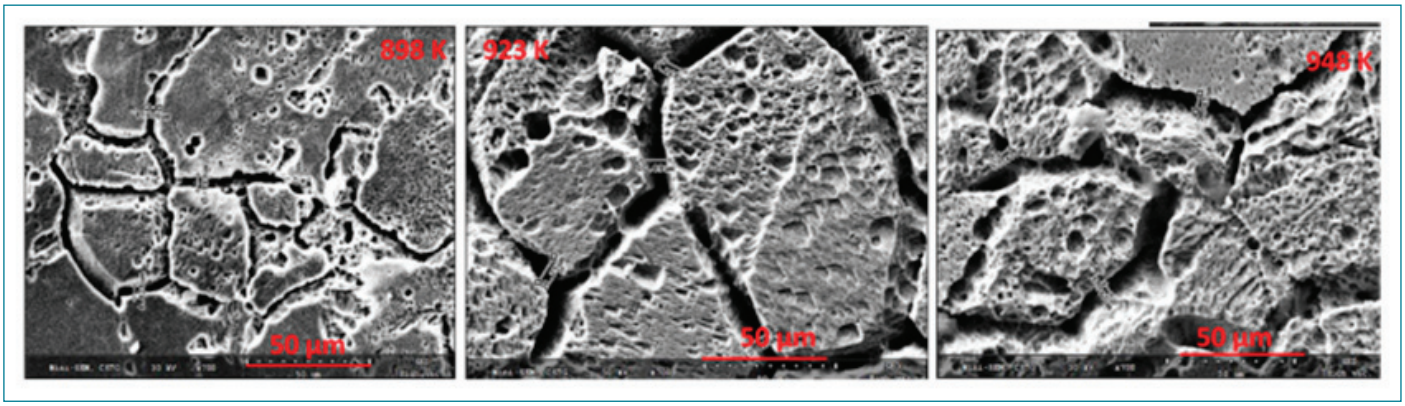

Fig. 2 SEM micrographs of 316LN SS sensitized at 898 K, 923 and 948 K showing grain boundary widths.

of 898 K, 923 K, and 948 K for 500 hours (The temperatures were chosen from the TTS diagram established for 316LN SS as shown in Fig. 1a), and the degree of sensitization (DOS) was determined using the DLEPR technique, yielding DOS values of 7.4%, 14.5%, and 9.3% for the respective sensitization temperatures (Fig. 1b).

Before EN measurements, a pulse polarization step was applied to isolate Cr-depleted regions in the sensitized grain boundaries for accurate EN signals as shown in Figure 1c. The correlation between DOS values from DLEPR and EN parameters, such as standard deviation of current (σI), and shot noise parameters such as characteristic charge (q), and characteristic frequency (fn), was established to assess the extent of IGC in different sensitized specimens.

The σI versus time plot indicated the highest values for specimens sensitized at 923 K, indicating severe IGC with significant grain boundary dissolution (Figure 1d). In contrast, specimens sensitized at 898 K showed lower σI values, signifying reduced dissolution and milder IGC. Those heat-treated at 948 K displayed intermediate dissolution rates. The calculated charge values (q) were 1.3, 15, and 4.3 mC for specimens heat treated at 898 K, 923 K, and 948 K respectively. The plot shown in Fig. 1e showed a good correlation ($r^2 = 0.99$) of the charge values evaluated from the EN technique and DOS value determined from the conventional DLEPR technique. The shot-noise parameter showed maximum metal loss per corrosion event (q/fn) for 316LN SS specimen sensitized at 923 K compared to that observed in the specimens sensitized at 948 and 898 K (Fig 1f). The trend observed in the results of shot-noise analysis was consistent with the DOS values obtained during conventional DLEPR tests.

The SEM observations further supported these findings wherein the 316LN SS sensitized at 923 K for 500 h showed highest grain boundary width of 10.22 ± 0.98 μm followed by the specimens sensitized at 948 and 898 K which showed grain boundary width of 6 ± 0.92 and 5.15 ± 0.67 μm respectively (Fig 2).

3. Effect of Nitrogen on the Pitting Corrosion of Stainless steel using Electrochemical Noise

The impact of nitrogen on 316L SS pitting corrosion was explored using EN signals analyzed via Wavelet analysis in 0.01 M FeCl3 for 24 hours. In wavelet transform, EN data is decomposed into different sets of wavelet coefficients (crystal) which contain information about corrosion events occurring at determined time scale. Small time scale process (crystal d2 and d3) represents uniform corrosion or passivation, medium time scale process (crystal d4 to d6) is linked to metastable pitting and large-scale processes (crystal d7 and d8) is linked to overlapped transients or stable pitting.

The time scales as well as frequencies for different detail crystals is given in Table 1.

Table 1. The time scale and frequencies for different crystals.

Crystal	Scale's	Frequency, Hz
d1	(2,1)	(0.5, 1)
d2	(4,2)	(0.25, 0.5)
d3	(8,4)	(0.125, 0.25)
d4	(16,8)	(6.25×10^{-2}, 0.125)
d5	(32,16)	(3.12×10^{-2}, 6.25×10^{-2})
d6	(64,32)	(1.56×10^{-2}, 3.12×10^{-2})
d7	(128,64)	(7.81×10^{-3}, 1.56×10^{-2})
d8	(256, 128)	(3.91×10^{-3}, 7.81×10^{-3})

Four 316L SS alloys with varying nitrogen content (0.07, 0.12, 0.14, and 0.22 wt. percent nitrogen) exhibited reduced transients, longer transient lengths, and decreased current and potential noise signals with increasing nitrogen (Fig. 3a).

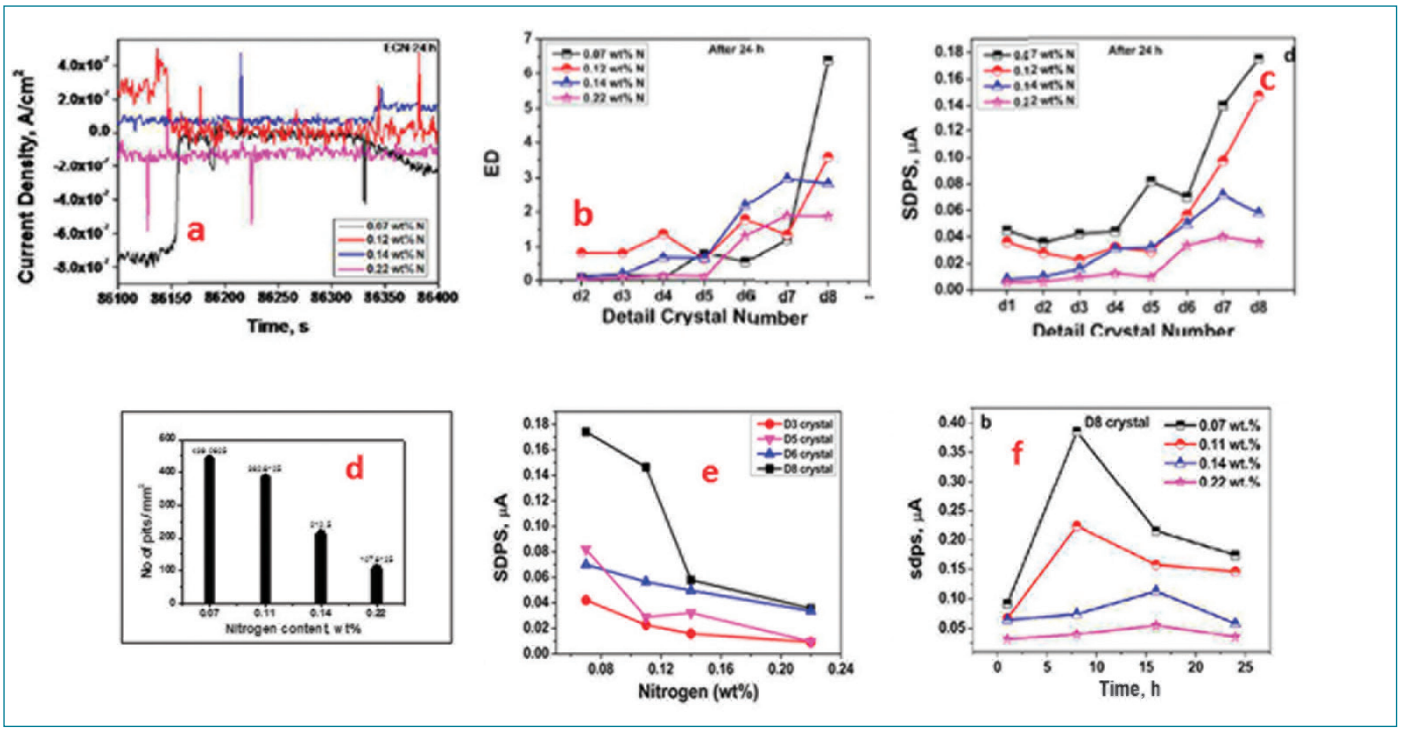

Fig. 3 ECN record (a), Energy distribution plot (b), SDPS plot (c) for different nitrogen containing 316L SS specimens after 24 h exposure, pit density plot (d), SDPS plots showing the variation of detail crystal d3, d5, d6 and d8 as a function of nitrogen (e), SDPS plot showing the variation of detail crystal d8 as a function of exposure time (f).

Wavelet analysis indicated reduced low-frequency signal energy with added nitrogen, suppressing long-time transients (Fig.3b). Dominant transient duration shifted from 16-32 seconds at 0.07 wt. percent nitrogen to 8-16 seconds with higher nitrogen, as shown by SDPS plot in Figure 3c (position of maximum peak between d1 to d5 crystal indicate dominant transient). The slope after the maximum peak in SDPS plot give information about the frequency of occurrence of the dominant transient. SDPS plot showed highest slope value for low nitrogen containing 316L SS. The slope value decreased with increase in nitrogen content, indicating decrease in pit density with increase in nitrogen content. This observation was confirmed from pit density calculation using image analysis which was found to be 439 ± 8, 383 ± 6, 212 ± 6 and 108 ± 4 pits/mm2 for specimen containing 0.07, 0.11, 0.14 and 0.22 wt.% nitrogen respectively (Fig 3d). Hence, the pitting tendency of the 316LN SS can be differentiated using wavelet analysis.

A clear decrease in the SDPS values for each crystal was observed as a function of nitrogen content (Fig. 5e). The SDPS value for low frequency signal (d8 crystal) was found to be highest for alloy 0.07 wt% N and with increase in nitrogen content, the SDPS value decreased. The SDPS value for high frequency signal (d3) did not show considerable variation in value with added nitrogen. This result showed that added nitrogen highly influenced the low frequency signal and showed little effect on the high frequency signal. The plots of d8 showed initial increase after 8 h exposure and subsequent rapid fall as a function of time due to buildup of strong passive film with time on the surface of SS (Fig. 3f). The sdps value of d8 decreased with increase in N.

CLSM showed reduced pit sizes with higher nitrogen content (Fig. 4). Pit radii ranged from 10-20, 10-17, 5-12 and 5-9 μm whereas pit depths were 72 ± 2, 60 ± 2, 54 ± 1 and 27 ± 1 μm for 316L SS containing 0.07, 0.11, 0.14 and 0.22 wt.% nitrogen respectively. As a result, it can be deduced that as the nitrogen level in the 316L SS increased, the pit diameter and depth reduced.

4. Pitting corrosion studies on different Mo containing SS using electrochemical noise technique

Pitting corrosion studies on stainless steels with varying molybdenum content: 0.02 wt.% Mo (304LN SS), 2.53 wt.% Mo (316LN SS), and 3.58 wt.% Mo (317LN SS) were conducted in 0.01 M FeCl3 at room temperature. Pitting corrosion potential (Epit) value increased with increase in Mo content, indicating the beneficial effect of Mo in increasing the resistance to pitting corrosion (Fig. 5a). ECN record showed large fluctuation in current signal in 304LN as compared to Mo containing SS (Fig.5b). Increasing Mo content reduced total current transients and decrease in transient with high current amplitude (Fig 5c), indicating enhanced pitting corrosion resistance. Shot noise analysis revealed varying maximum charge values (q), with 316LN and 317LN SS exhibiting significantly lower pit currents than 304LN SS (Fig 5d).

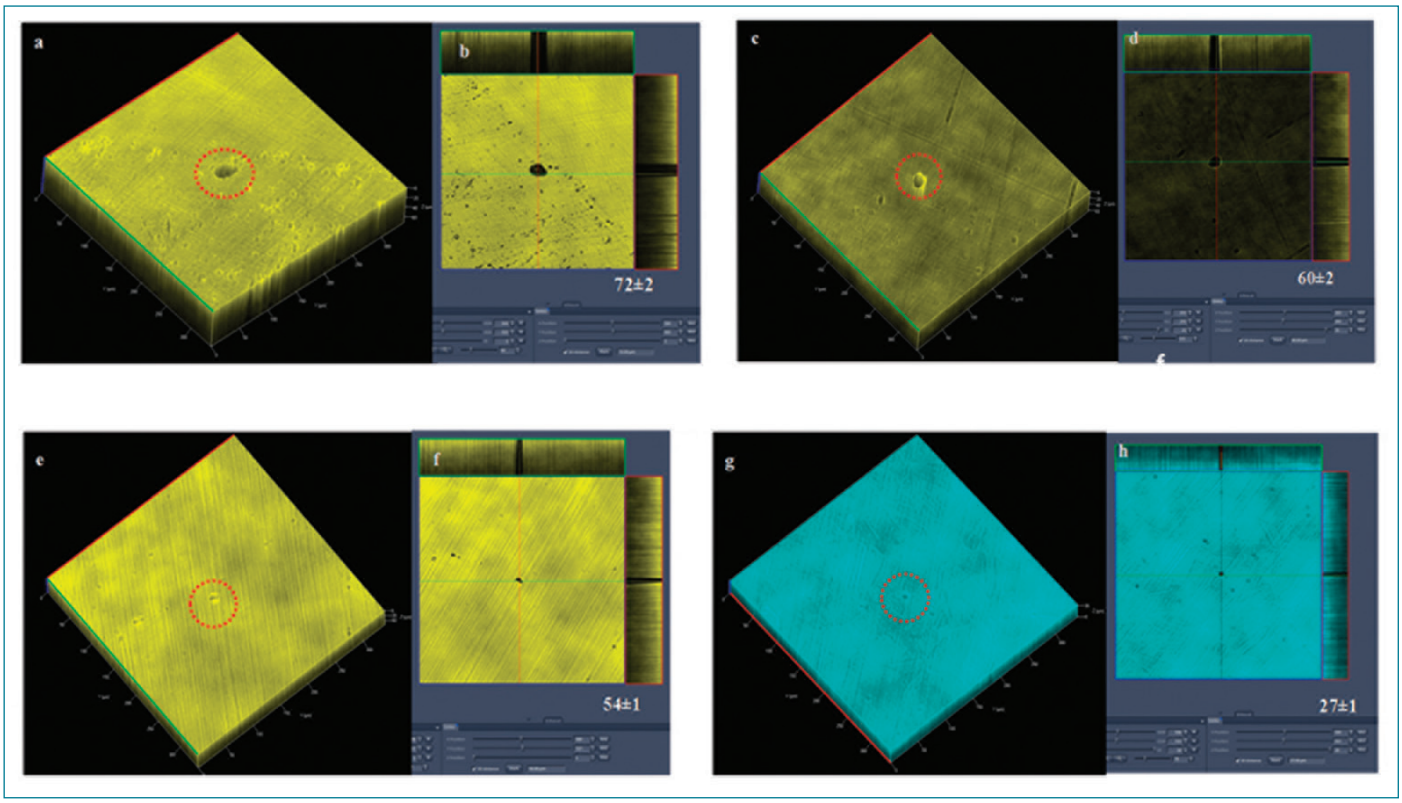

Fig. 4 CLSM micrographs of pits showing the respective 3-D and orthogonal views of (a-b) 0.07 wt.% (c-d) 0.11 wt.%; (e-f) 0.14 wt.%; and (g-h) 0.22 wt.% N.

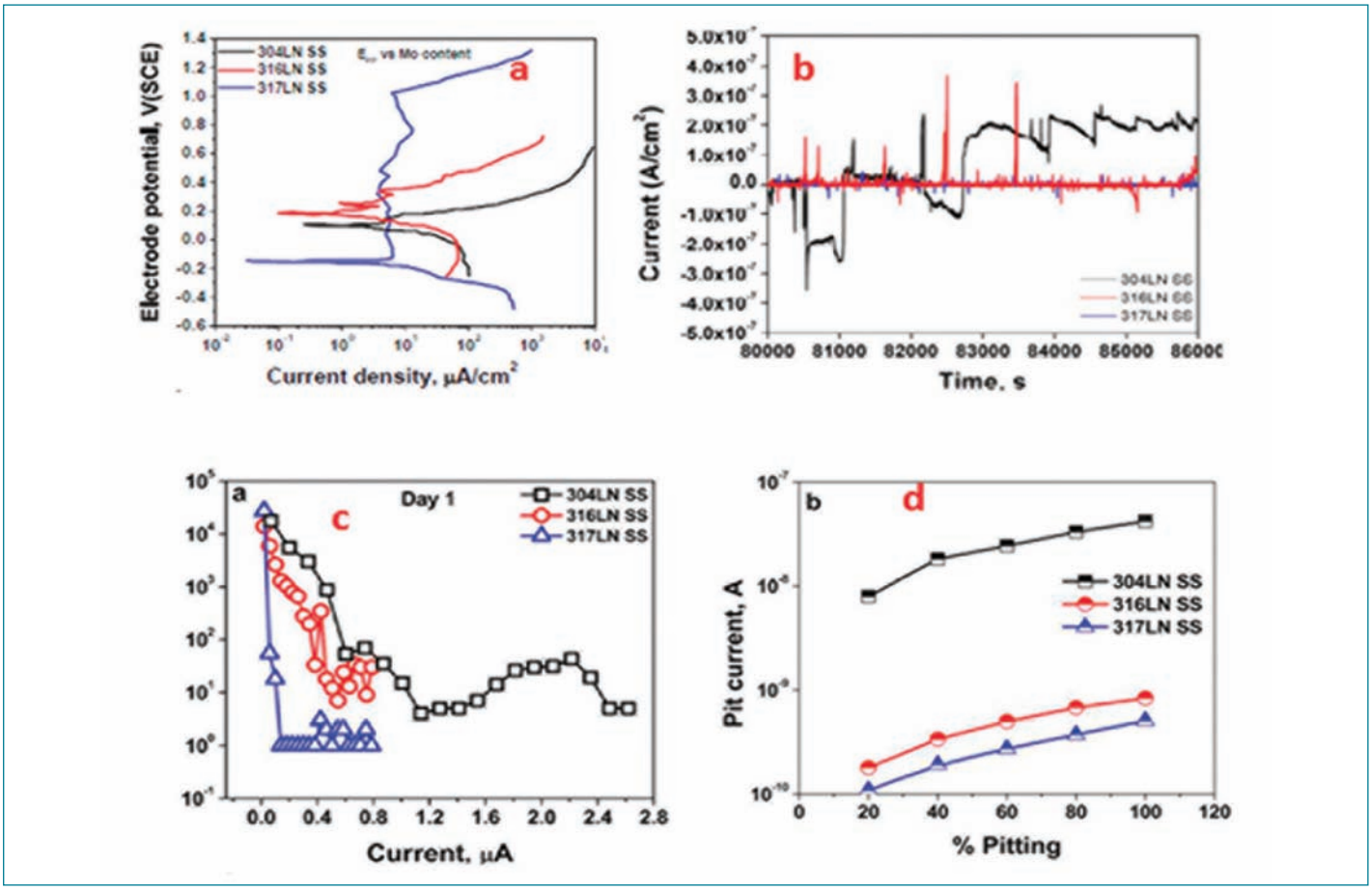

Fig. 5 Potentiodynamic polarization curve (a), Visual record for ECN signals (b), The current transients plot after day 3 of exposure (c), Pit current vs. % pitting plot (d).

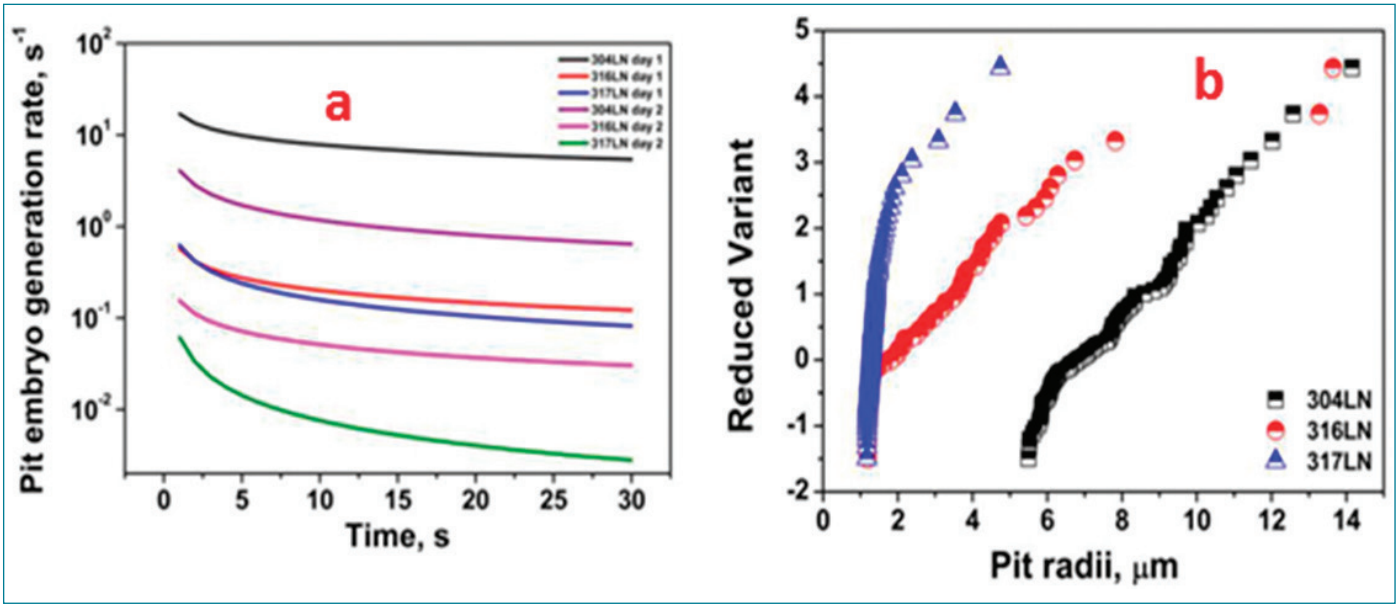

Fig. 6 Plot of pit generation rate for 304LN, 316LN and 317LN SS after exposure for 24 and 48 h (a), Gumbel probability plots for pit radii in 304LN, 316LN and 317LN SS (b).

Longer pit initiation times for 316LN and 317LN SS demonstrated Mo's effect in delaying pit initiation (Table 2).

Table 2. Mean free time for pit initiation in 304LN, 316LN and 317LN.

Specimen	Duration of exposure, hr	Mean-free time for pit initiation, s
304 LN SS	24	1.6×10^{-3}
	48	4.3×10^{-3}
	72	0.042
316 LN SS	24	1.31×10^{-3}
	48	5.6×10^{-3}
	72	1.66
	24	0.87
317 LN SS	48	0.93

Pit generation rates from Weibul plot were observed to be lower for 317LN and 316LN alloys as compared to 304LN (Figure 6a). The pit initiation rate follows the given order: 304LN >316LN >317LN. The Gumbel plot for pit radii showed lowest metastable pit radii in 317LN SS and the highest in 304LN SS. The maximum size of metastable pits obtained using Gumbel plot in 304LN, 316LN and 317LN ranged from 1-10, 1-16 and 12-28 μm respectively (Figure 6b).

Surface characterization using XPS and LRS detected Mo-oxides and Cr spinels in the passive film of Mo containing SS, enhancing pitting corrosion resistance. CLSM showed the formation of shallow pits in the Mo containing SSs which could be attributed to the presence of Mo oxides (MoO3), and Cr spinels (FeCr2O4, Fe2(CrO4)3) in the passive film of 316LN and 317LN SS. These spinels and Mo-oxides acted as a barrier for initiation of pitting corrosion in the highly aggressive chloride containing medium limiting pit propagation and facilitated repassivation of pits.

Young Researcher's Forum

Shri S. Kumar is working as a Research Scholar in Radiation Application & Metrology Section, RESD, SQRMG, IGCAR. He acquired Bachelor degree in Mechanical Engineering from Anna Univeristy, Chennai and Joined IGCAR 2014, registered his Dual Degree Programme (M.Sc (Engg) and Ph.D) in HBNI under the guidance of Dr. B. Venkatraman. He obtained his M.Sc (Engg) degree in 2017 on the title "Evaluation of Weld Joints in DFRP Tanks by using various NDE methods – Experimental and Simulation". In addition, he was completed his Ph.D. under the broad field of Phased ultrasonic testing and the project entitled "Phased array ultrasonic testing of dissimilar weld joints – Modelling and Experiments". He has published three papers in peer-reviewed international journals of his Ph.D work and attended four conferences.

Effect of Attenuation and Beam Skewing of Ultrasonic Beam in Nuclear Component Materials

1. Introduction

Prototype Fast Breeder Reactor (PFBR) is a 500MWe pool type, sodium-cooled nuclear reactor, which is second stage programme. It consists of reactor main vessel, inner vessel, intermediate heat exchangers, Steam generators, Sodium pumps and pipes which are made by different materials. The dissimilar weld joint is fabricated between the main pipelines (SS 316L (N)) and the structural material (P91) used in the steam generator is of very critical concerned to the sodium-water interactions. Such dissimilar joints suffer from a mismatch in coefficients of thermal expansion (CTE) and the migration of carbon from the P91 to the austenitic steel during service. In general, this is overcome using the nickel-based consumables during welding of such dissimilar joints. The use of a tri-metallic combination with an insert piece of intermediate

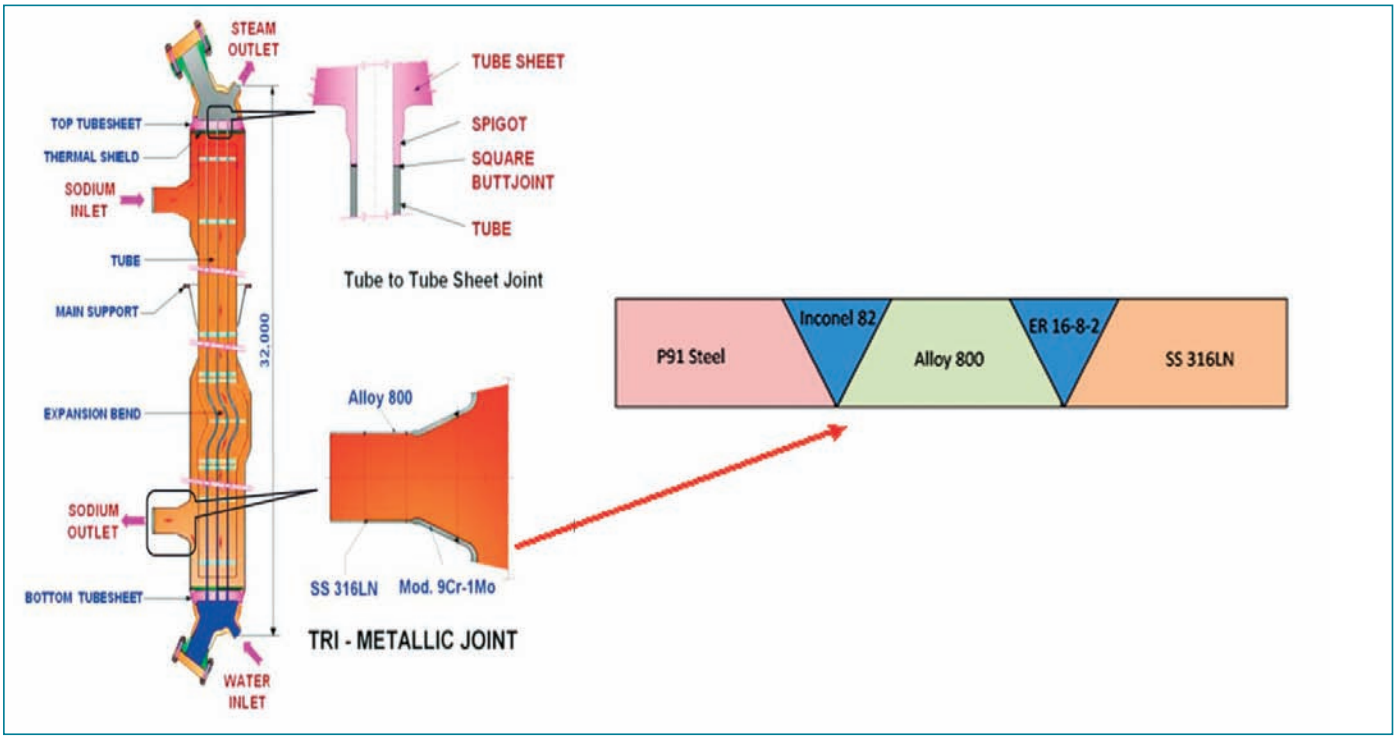

Figure 1: Schematic arrangement of Steam Generator in PFBR and Trimetallic weld joint.

CTE lowers the thermal stresses. Steam generator is made up of Tri metallic configuration joint, the transition piece (Alloy 800) is placed between the Ferritic steel (P91) and austenitic stainless steel (SS316LN). Trimetallic weld joint configuration of PFBR is shown in Figure 1. Steam generators are the workhorses in nuclear power plant. PFBR has eight Steam Generators. This steam generator is connected with IHX. Any leaks in sodium systems have the possibility of being exceptionally hazardous due to the reaction of liquid sodium with oxygen and water vapour in the air. It is one of the most critical components governing the safe and efficient running of the plant. Welds are critical area in the materials and failure occurs in during fabrication or in-service which will leads to financial and environmental losses. So, it is an important requirement from the viewpoints of safety and economics to check the integrity of the welds.

Non Destructive Evaluation (NDE) as the name imply, is the technology of assessing condition and performance of material, component or structure without impairing its functional properties. Among several complementary NDE methods, radiography and ultrasonic methods are widely used for the volumetric evaluation of weld joints. Ultrasonic Testing (UT) is a volumetric non-destructive evaluation most popularly used in the plant for quality control of the nuclear components. Due to the propagation of an acoustical wave through material, the received signal provides the information on the mechanical or the physical properties of the components. Ultrasonic inspection is very challenging due to beam skewing, dispersion, unexpected attenuation by material microstructure. The microstructure of the materials affects the ultrasonic beam propagation and increase the backscattering noise due to the attenuation. Phased array ultrasonic techniques (PAUT) offer significant technical advantages over conventional ultrasonic because of the electronic beam steering, multi-angle scanning and dynamic depth focusing capabilities. PAUT involves the utilization of multi-element transducers which is capable of generating multiple angles at a focused point. As a result, using a single phased array probe, defects of any orientation can be detected. Recently, the dual matrix array (DMA) probes based on the Transmit-Receiver Longitudinal (TRL) technique is introduced for the testing of coarse grained materials and heterogeneous weld joints. The DMA probe has a two-dimensional arrangement of elements in square or chessboard pattern. The transmitter and receiver elements are acoustically insulated which eliminates the wedge internal reflection echoes associated with the pulse-echo technique without requiring a damping material. In addition, a smaller wedge generates less attenuation and helps in increasing the focus depth of the probe in the material. The design of the squint and roof angle allows the focusing at a point inside the material and generates a pseudo-focalization. This pseudo focusing helps in receiving signals from a limited volume where the transmitter and receiver beam overlap which enhances the sensitivity of defect detection. A review of the literature reveals that very limited work has been carried out on the investigation of coarse grain materials using DMA probes. The present paper describes the attenuation of ultrasonic beam and measurement of attenuation for Modified 9Cr-1Mo (P91), SS316LN and Alloy 800 base metals by different frequency. This paper also presents the comparison of phased array probes in the weld blocks by scattering, beam skewing and signal to noise ratio. The weld samples are fabricated by Gas Tungsten Arc Weld (GTAW). The specimens have been examined for their microstructure feature which includes grain size and orientation.

2. Theory of Ultrasonic attenuation

Ultrasonic beam propagated through the material, amplitude and intensity of sound energy decrease as it travels. Energy losses occur due to absorption and scattering. The energy loss due to absorption is a result of mechanisms such as thermo elastic effects, hysteresis losses, dislocation damping, etc. Scattering losses in polycrystalline materials are depends on the ratio of grain size (D) and wavelength (λ). The attenuation coefficient is calculated by finding the difference of amplitude (dB) between the two signals on the back surface and then dividing it by the total path traveled. It is expressed in terms of dB/mm. The energy loss of ultrasonic waves in materials can mainly caused by the spreading, absorption and scattering of ultrasonic waves. The following equation will express the attenuation caused by absorption and scattering.

$$AR = A_0 \cdot e^{-\mu \cdot t}, \qquad (1)$$

Where, the amplitude of the received ultrasonic waves is AR, attenuation coefficient is α, and the propagation time is t. According to different attenuation mechanisms, the attenuation coefficient can be divided into several sections that can be expressed as

$$\mu = \mu_S + \mu_A, \qquad (2)$$

Where, the attenuation coefficient due to scattering is μS, the attenuation coefficient due to absorption is μA. The attenuation coefficient due to absorption is usually very small and can be ignored. The principle of wave scattering from the grains fulfills the following premises: The number of scatters is inversely proportional to mean grain volume assuming cubic grain structure. The elastic modulus variation is much smaller than the mean modulus and the alloy is single phase and consists of equiaxed grains schematically shown in Figure 2. The attenuation coefficient due to grain scattering is closely related to ratio of the wavelength (λ) and grain size (D). Generally, it can be divided into three regimes, summarized in Table 1. Where the volume of grains is Vg, the frequency of ultrasonic waves

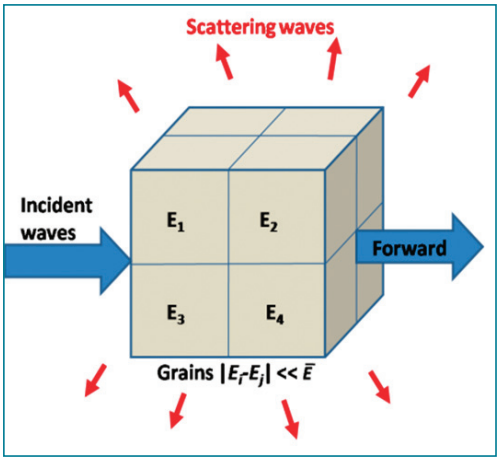

Figure 2. Schematic drawing of grain scattering

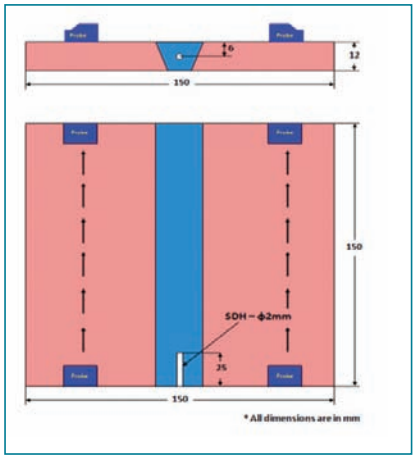

Figure 3. Schematic drawing of weld sample

Figure 4. Ultrasonic immersion system

is f and constants related to material properties are K1, K2, and K3.

Table 1: Classification of scattering type

Relationship	Scattering Regime	Attenuation Coefficient (μ)
$\lambda > 2\pi D$	Rayleigh	$\mu = K_1 V_g^3 f^4$
$\lambda \approx 2\pi D$	Stochastic	$\mu = K_2 D f^2$
$\lambda << 2\pi D$	Geometric	$\mu = K_3 D^{-1}$

3. Experimental Analysis

3.1 Material Details

The present study involves three different material samples, namely Modified 9Cr-1Mo (P91), Austenitic steel (SS316LN), Alloy 800. The chemical compositions of materials are shown in Table 2. The reference block made of above materials was fabricated by the GTAW process. The thickness of base material, root face and root gap are 12 mm, 1 mm and 2 mm respectively. The dimensions of the weld samples are 150 mm X 150 mm X 12 mm as indicated in Figure 3. In the reference block, artificial reflector such as Side Drill Hole (SDH) of diameter 2 mm and 25 mm length were machined at a depth of 6 mm from the top surface of the weld was created by electro-discharge machining (EDM) process for beam skewing calculation.

3.2 Microstructure details

The microstructural features are characterized using metallographic specimens which are cut from the samples involves grinding, electro-polishing and etching. The P91 material was etched using Nital (10 ml nitric acid + 100 ml ethanol) and Alloy 800 & SS316LN were etched using Kalling etchant (5 gm CuCl2 + 100 ml HCL + 100 ml Ethanol). In this process microstructure from the base metal zone, weld zone could be observed.

3.3 Ultrasonic parameters

The experimental setup of attenuation, as shown in Figure 4, consists of a C-scan system comprising of an immersion tank filled with water and a 5-axis scanner controlled by a Lab VIEW based software. Olympus 5077PR Square wave pulser/receiver and a PCI-based digitizer card placed in the C-scan system were used for acquiring the ultrasonic signals. An unfocused ultrasonic probe with a frequency of 2.25 MHz, 3.5 MHz, 5MHz, and 10MHz was used for data acquisition. Beam skewing and Signal to noise ratio for different materials is calculated using LA probes and DMA probes. The data acquisition system was composed of the omniscan MX2 device and omniscan PC software that were supplied by Olympus, USA. Parameters of the LA and DMA probes are shown in Table 3.

Table 3: Probe details

Category	Parameters	
Probe	LA probe	DMA probe
Array type	1D Linear array	2D Matrix array
Number of elements	16	16X2
Centre frequency	5MHz	5MHz
Total active area	9.6mm	16X6
Refraction angle	60, 55	55
Wedge type	SA10-N60L, SA10-N55S	SA27-DN55L, DNCR

Table 2: Chemical composition (wt. %) of the P91 and Alloy 800

	C	Cr	Ni	Mo	Mn	P	S	Si	Ti	Cu	Fe
P91	0.082	8.39	0.39	0.87	0.38	0.008	0.001	0.26	<0.005	0.2	Bal
Alloy 800	0.075	19.159	30.56	-	1.17	0.01	0.002	-	0.54	0.62	Bal
SS316LN	0.025	17.9	12.1	2.4	1.8	0.03	0.002	0.31	0.54	0.62	Bal

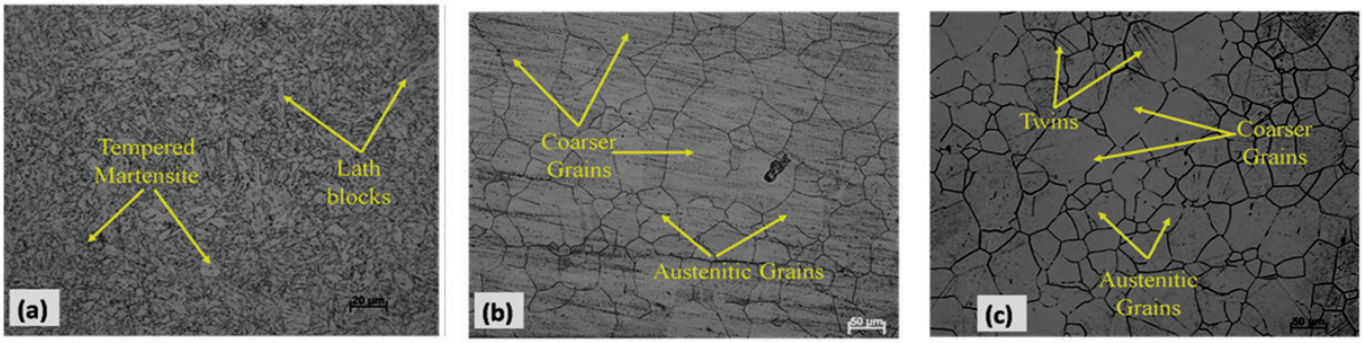

Figure 5: Microstructures of (a) P91base metal (b) SS316LN base metal (c) Alloy 800 base metal

4. Results and Discussion

4.1 Metallographic analysis

The microstructure of the base material Alloy 800 is shown in Figure 5(a). The Alloy 800 has equiaxed grains of austenite with several twinning observed in the microstructure. It consists of microstructure with solid solution matrix in which some grains are outlined by the precipitate particles at the boundaries and by twining lines which are shown in Figure 5(a). Very large coarse grain is observed in the alloy 800 side in the range of 50 μm to 80 μm. The microstructure of the received base material P91 is shown in Figure 5(b). The microstructure of P91 consisted of tempered lath martensitic structures. The average grain size found by mean intercept method is about 24 μm as per ASTM No 8 method. The microstructure of the stainless steel 316 has equiaxially annealed austenitic grains with twins and a small amount of delta ferrite in the form of stringers. The base metal shows the microstructure with grains in the range of 25–60 μm (Figure 5(c)). The size, the arrangement and the elastic anisotropy of the different grain result in high scattering associated with mode conversion effects, beam distortion, and a variation of ultrasonic velocity with direction and position in the weld. The scattering energy is observed as a relatively high noise level end high attenuation.

4.2 Attenuation results

The technique used in the present measurements is the pulse-echo technique where rf pulses are fed to a single quartz crystal transducer which acts as the transmitter as well as receiver

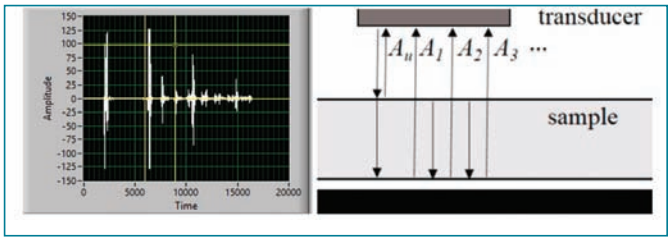

Figure 6. (a) Typical A scan (b) Sound wave propagating to the medium

of acoustic pulses. The received waveforms were recorded automatically by the system by using an oscilloscope. The acoustic attenuation is determined from the two primary echoes received from signal. A typical A-scan image with these echoes for Alloy 800 is shown in Figure 6(a). The signal marked Au is reflected from the upper surface of the sample (out of the range of display), while the signals marked A1, A2, and A3 are back-wall waveforms reflected from the bottom side of the specimen is shown in Figure 6(b).

The amplitude of the signals reflected from the upper surface Au could be considered the same because the amplitude of the incident waves and the distance from the focused transducer to the upper surface of specimen are the same. However, the amplitude of the signals reflected from the bottom surface (A1, A2, and A3) show significant differences owing to variations in the grain sizes of the specimens. Therefore, the scattering of ultrasonic waves due to grains is different in various materials. The attenuation coefficient due to grain scattering can be calculated from the amplitude of the back wall signals. The attenuation coefficient is measured by finding the amplitude difference (dB) between the two back surface signals and then dividing it by the total path travelled. It is expressed in terms of dB/mm. Figure 7 shows the A scan image of alloy 800, SS316LN, P91 materials at 5MHz.

Table 4: Attenuation (dB/mm) for different material

Frequency	Materials		
	P91	SS316LN	Alloy 800
2.25	0.19	0.23	0.25
3.5	0.16	0.19	0.27
5	0.11	0.17	0.27
10	0.13	0.23	0.38

The relationship between the attenuation coefficient and the frequency of the incident waveforms for different materials is shown in figure 8. For SS316LN, frequency of the incident waveforms in

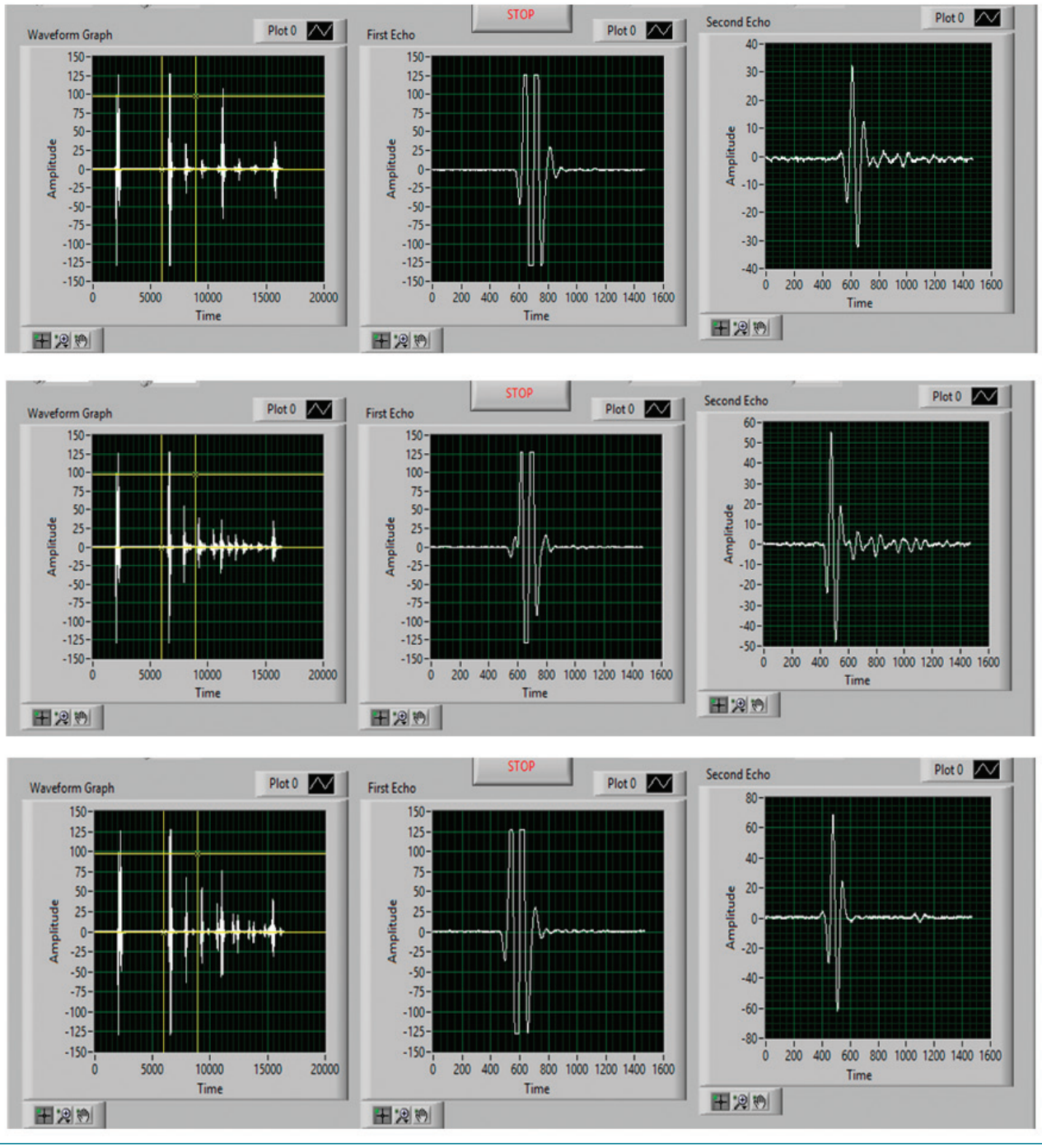

Figure 7. Examples of waveforms received from various samples at 5MHz: (a) Alloy 800 (b) SS316LN (c) P91

the experiments ranges from 2.25–10 MHz; thus, the wavelength of the ultrasonic waves ranges from 600–2670 μm. The grain sizes were measured from 2D cross sections. However, the grain sizes used in the ultrasonic scattering theory should be three-dimensional (3D) values. Therefore, it is necessary to calibrate the measured 2D average grain size to an equivalent 3D value D3. Here, a factor of two was adopted to multiply the 2D average grain size . As a result, 2πD3 ranges from 300–860 μm, the magnitude of which is lower to that of the wavelengths of the incident waveforms in the experiments. Therefore, the scattering due to grains in the present study is located in the Rayleigh scattering regime. The relationship between the attenuation coefficient and frequency in the Rayleigh regime for SS316, the inhomogeneous grain size distribution may also play a dominant role. As the frequency of ultrasonic wave increases, their wavelength decreases. The wavelength tends gradually towards the size of large grains and then to that of small grains, which represent entry into and exit from the Rayleigh scattering regime, respectively. According to the Rayleigh scattering theory, the attenuation

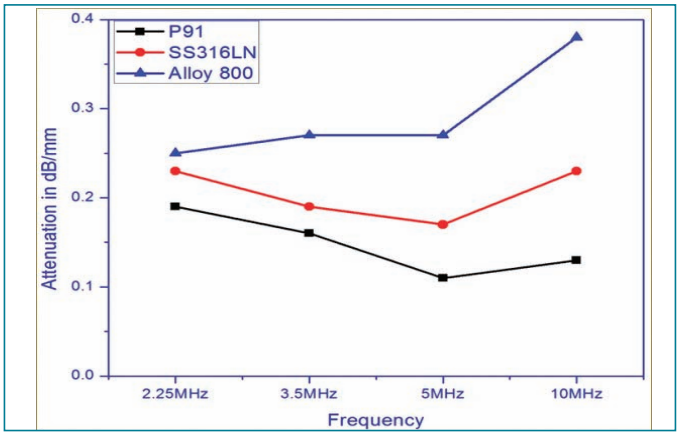

Figure 8. Graphical representation of attenuation value for different materials

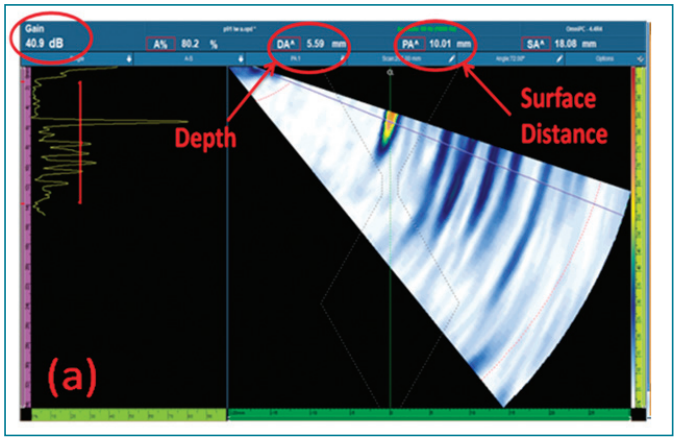

Figure 9 : The calibration of reference weld block (Detection of SDH)

coefficient is proportional to both grain size and frequency. If grain size distribution was homogenous, it would be easy to understand that the attenuation coefficient is dependent solely on the frequency. Supposing that the grain size differs largely, it is also reasonable to assume that the large grains determine the attenuation coefficient at the beginning of the Rayleigh scattering regime, whereas the relatively smaller grains determine the attenuation coefficient at the end of the Rayleigh scattering regime. Therefore, although the wave frequency increases from the beginning to the end of the Rayleigh scattering regime, the larger attenuation coefficient obtained at the beginning can be attributed to a considerably larger grain size.

4.3 Scattering due to different grain structure

The side drilled hole of diameter 2 mm made at the centre of the weld has been used as the reference standard and the phased array equipment was calibrated based on the reflected echo from SDH with the echo amplitude at 80% of the full screen height. Figure 9 shows the calibration of weld reference block (Detection of SDH). The energy required (Gain) to maintaining the reflected amplitude at 80% from the SDH for different transducers were tabulated in Table 5. It can be observed from the Table 2 that low gain energy (dB) is required while scanning from P91 material compared to SS316LN and Alloy 800. Scattering is less for P91 material which is a fine grain structure. High energy loss (Scattering) is taken place in the Alloy 800 material which is a coarse grain structure. So, more gain is required for detecting the side drill hole at 80% amplitude. Scattering is directly proportional to the mean grain size and inversely proportional to the wavelength. Longitudinal wave is less suffered in scattering due to wavelength effect (approx. twice the shear wavelength) and reduces the noise. But Longitudinal wave is required more gain due to the wedge height. DMA probe requires less gain for detecting the hole compared to LA probe. DMA probe with LW have better focusing in the material. DMA probe provides the pseudo focusing that eliminates the dead zone and backscattering signal. The gain obtained from experimental study of the block is used for beam skewing studies on weld sample.

Table 5: Gain (dB) required for detecting hole depth in different material

Probes	Materials		
	P91	SS316LN	Alloy 800
LA Probe with SW	32	38	55
LA Probe with LW	35	42	60
DMA probe with LW	30	36	42

4.4 Beam skewing

We are using phased array beam probes to study the beam skewing. The probe is placed on the material after applying couplant and the signals of the oscilloscope screen are noted. For particular distance of hole the beam path was noted on the basis

Table 6: Beam skewing for P91 material

Probes	Hole Depth (mm)	Angle (Deg)	Calculated beam path (mm)	Obtained Beam path (mm)	Difference in Beam path (mm)	Single to Noise ratio (SNR)
LA Probe with SW	6	45	8.48	8.67	0.19	20
		60	12	12.29	0.29	16
LA Probe with LW	6	45	8.48	8.66	0.18	25
		60	12	12.26	0.26	19
DMA probe with LW	6	45	8.48	8.63	0.15	28
		60	12	12.22	0.22	23

Table 7: Beam skewing for SS316LN material

Probes	Hole Depth (mm)	Angle (Deg)	Calculated beam path (mm)	Obtained Beam path (mm)	Difference in Beam path (mm)	Single to Noise ratio (SNR)
LA Probe with SW	6	45	8.48	8.83	0.35	14
		60	12	12.48	0.48	10
LA Probe with LW	6	45	8.48	8.76	0.26	17
		60	12	12.36	0.34	15
DMA probe with LW	6	45	8.48	8.68	0.20	22
		60	12	12.27	0.27	19

Table 8: Beam skewing for Alloy 800 material

Probes	Hole Depth (mm)	Angle (Deg)	Calculated beam path (mm)	Obtained Beam path (mm)	Difference in Beam path (mm)	Single to Noise ratio (SNR)
LA Probe with SW	6	45	8.48	8.96	0.48	10
		60	12	12.71	0.71	8
LA Probe with LW	6	45	8.48	8.84	0.31	13
		60	12	12.43	0.39	10
DMA probe with LW	6	45	8.48	8.71	0.23	16
		60	12	12.35	0.35	14

line of the oscilloscope. We have the actual whole depth. Using this, calculated Beam path is related to the observed beam path. The differences are obtained in the whole depth for different blocks at different depths. The calculated beam path is given by the formula as

Beam path $= t/\cos\theta$

Where, t –thickness of the specimen

The ultrasonic beam skewing results of the P91, SS316LN, Alloy 800 materials are calculated and tabulated in Table 6, 7, 8. Difference in beam path is higher for shear wave compared to longitudinal wave. This beam path difference increases with increasing the sound path length. Beam path difference is high for alloy 800 material due to coarse grain microstructure. Weld metal exhibits a structure with bent dendrites depending on the welding parameters and the conditions during solidification. This weld structure will produce anisotropy of the plane perpendicular to their axes, and also lead to the deflection of ultrasound beams because the wave fronts are no longer necessarily normal to the propagation direction. For shear waves, the skewing effect is greater than longitudinal wave due to the wave length. The wavelength of the shear wave is lower than longitudinal wave (approximately half of the wavelength). For shear waves, the signal from the fusion face is greater than that for a side drilled hole in weld metal whereas the reverse is true for longitudinal waves. There is large velocity difference between the base metal and weld metal. Thus the acoustic impedance mismatch at the fusion boundary is larger for the shear waves than for the longitudinal waves.

4.5 Signal to Noise Ratio (SNR)

Scattering increases with grain size, frequency and elastic anisotropy and also depends on the material properties, density and sound velocity. Figure 10 shows SNR value for P91, SS316LN & Alloy 800 materials using different types of probes. A wide sound beam will lead to a worse signal to noise ratio because of the greater volume of scattering grains. SNR value is higher for P91 material which is fine grain structure whereas low for Alloy 800 and SS316LN material due to coarser grain structure. A reduction of the scattering volume is obtained by the use of focusing or twin crystal transducers which generate narrow beams. A significant amount of energy loss occurs because of wedge attenuation. LA probe uses a large wedge with dampening material which causes the loss of ultrasonic energy whereas DMA probe designed to smaller wedge without dampening material which provides maximum sound field into the material. The SNR is directly related to the shape and size of the focal spot/focusing. DMA probe possesses less distortion of the sound beam which leads to better focusing and the energy is more concentrated at the focal spot. In case of LA probe, the acoustic beam gets distorted severely and the focal length becomes narrower and possesses a poor focusing effect. The transmitter receiver principle enhances the signal to noise ratio and retains the sound field better than pulse echo transducer. DMA

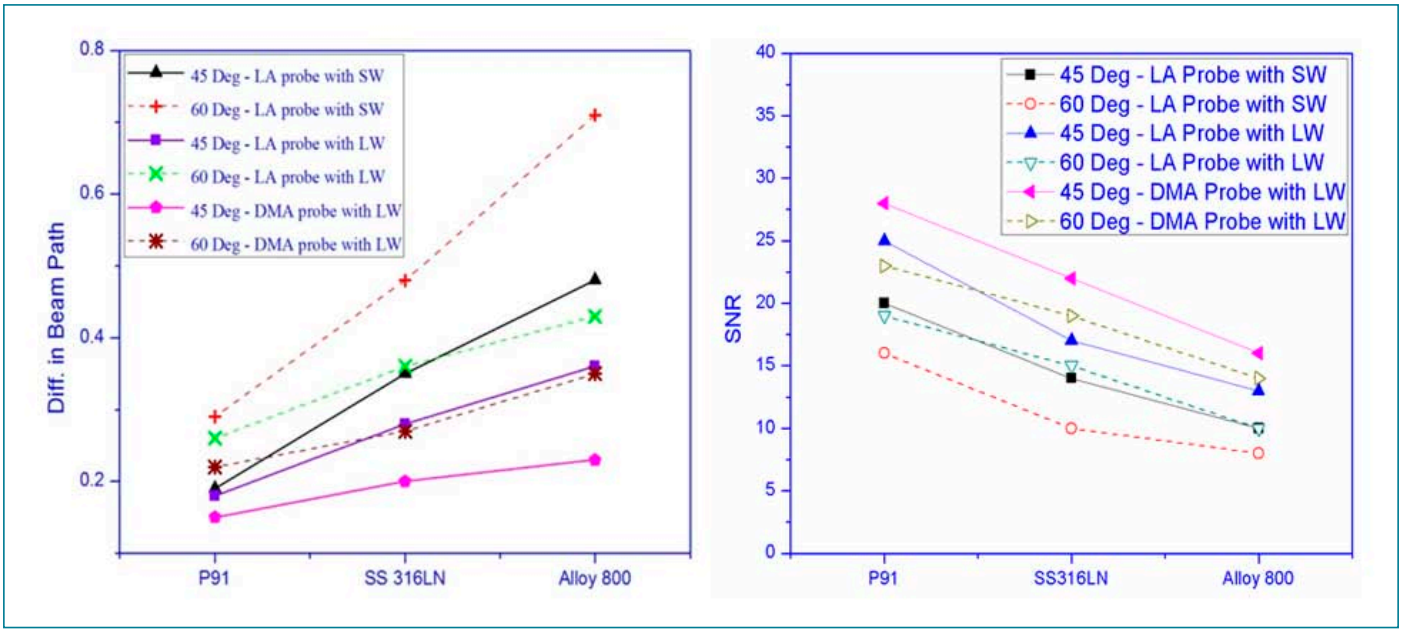

Figure 10. Beam skewing and SNR for different types of materials

transducer has advantage over a LA transducer due to its excellent depth of focusing in welds and increases the sensitivity towards detection of smaller defects. The DMA Probe also eliminates the echo interface, decreases backscattering signals which allow the use of higher gain.

5. Conclusions

This paper has presented effect of attenuation and beam skewing of ultrasonic waves in P91, SS316LN, and Alloy 800 materials. Attenuation of ultrasonic waves is carried out on the material using different frequency. It is observed that 5MHz probe giving less attenuation for P91& SS316LN materials. Rayleigh scattering is observed for the above materials. According to the Rayleigh scattering theory, the attenuation coefficient is proportional to both grain size and frequency. Scattering experiment is studied for different grain structure materials. The increased grain size in alloy 800 materials shows the high energy loss compared to other materials. High scattering is taking place in alloy 800 material because of energy lost in the grain boundaries. Beam skewing is higher for shear wave compared to longitudinal wave due to the wavelength and acoustic impedance effect. The acoustic impedance mismatch is larger for shear wave compared to longitudinal wave. DMA transducer has better SNR than LA transducer with a value of 28, 22, and 16 for P91, SS316LN and Alloy 800 respectively. DMA probe shows better SNR, less beam skewing and scattering compared to LA probe due to the pseudo focusing principle which increases the sensitivity of smaller defects and eliminates the wedge reflection echoes & backscattering signals. DMA probes are suitable for the inspection of coarse grain materials and dissimilar welds.

Public Awareness Activity

July to September, 2023

1. Exhibition on 'The Fourth State' - Plasma & 'Atoms in the service of the Nation'

Institute for Plasma Research, Ahmedabad, Gujarat & Tamil Nadu Science and Technology Centre, Chennai, in association with Indira Gandhi Centre for Atomic Research (IGCAR), Kalpakkam, organised a 5-day exhibition on 'Nuclear technologies and its applications' at Birla planetarium, Chennai, from July 3 to 7, 2023. The objective was to create awareness about the key role of nuclear energy in the energy security of the nation and applied research in Plasma Science and Technologies. The mandate was to develop expertise for Nuclear Fusion, a source of energy with two major TOKAMAK experiments, including India's First Indigenous TOKAMAK 'Aditya'.

The exhibition was inaugurated on July 3 by Prof. Nilesh J. Vasa Dean, Indian Institute of Technology (M), Chennai. It saw a footfall of 2,741 till July 7.

2. Anu Awareness Yatra 2023

An awareness programme named 'Anu Awareness Yatra – 2023' with the theme 'ATOMS IN THE SERVICE OF THE NATION' was organised by IGCAR in association with the National Council of Science Museum (NCSM), Ministry of Culture, Government of India, Vigyan Bharathi - Arivial Sangam, Tamil Nadu, and Indian Association for Radiation Protection. The programmes were organised in nodal institutions in seven districts in Tamil Nadu and three in Kerala as part of Azadi Ka Amrit Mahotsav, and to showcase the indigenous progress in science and technology. The objective was to highlight (i) the progress in nuclear science and technology in India, popularise technologies developed by the Department of Atomic Energy (DAE) for societal application, and applications of ionizing radiation in various walks of life; (ii) to create an interest among the youth in science subjects and to explore opportunities in DAE; (iii) Dispelling myths on nuclear energy.

The curtain raiser was organised at IGCAR, Kalpakkam, on July 24, 2023. The yatra was flagged off by Ms. K. A. Sadhana, Director, Visvesvaraya Industrial & Technological Museum (VITM), and Shri Gopal Parthasarathy, State Secretary, VIBHA, (Tamil Nadu Arival Sangam), in the presence of Director, IGCAR and senior officials. Dr. Ajit Kumar Mohanty, Chairman AEC & Secretary DAE, addressed the gathering through a message. The yatra culminated at IREL, Aluva, travelling more than 1,000km, covering Kancheepuram, Thiruvannamalai, Salem, Erode, Karur, Coimbatore, Palakkad, Thrissur and Kochi. In each of these places, a nodal institution was chosen in association with Vigyan Bharathi – Tamil Nadu Ariviyal Sangam and an awareness programme was organised in that institution for two days. The nodal centres coordinated with regional institutions of each district to ensure the active participation of about 2,000 students and the public in each venue. The programme comprised lectures, quiz competitions, art competitions, creative writing competitions, conceptual orations, and exhibitions showcasing nuclear reactor models and the application of ionising radiation in medical, engineering, and agricultural fields.

Photographs during inauguration of exhibition on " The Fourth State" - Plasma & "Atoms in the service of the Nation"

Flag off of Anu Awareness Yatra at Indira Gandhi Centre for Atomic Research (IGCAR), Kalpakkam on 24 .07. 2023

Anu Awareness @ Sri Sankara Arts And Science College, Kanchipuram on 25.07.2023-26.07.2023

Anu Awareness @ Arunai Engineering College, Thiruvannamalai on 27.07.2023 – 28.07.2023

Anu Awareness @ AVS College of Arts & Science, Salem on 31.07.2023-01.08. 2023

Anu Awareness @ Erode Sengunthar Engineering college, Erode on 02.08.2023-03.08.2023

Anu Awareness @ Sri Sarada Nikaten College of Arts and Science, Karur on 04.08.2023-05.08.2023

Anu Awareness @ Kumaraguru Engineering College, Coimbatore, on 07.08.2023-08.08.2023

Anu Awareness @ NSS College of Engineering, Palakkad on 09.08.2023-10.08.2023

Anu Awareness @ Christ college, Iringalakuda during 11.08.2023 – 12.08.2023

Conclusion of Yatra at IREL (India) Limited, Aluva on 14.08.2023

Bala Vidya Mandir Senior Secondary School, Adyar, Chennai on 12.8.23 as part of the inter-school exhibition

This Yatra was unique in that a mobile science exhibition named "Science on Wheels" from VIT-M showcased working models on societal application of space technology. A total of 25,720 people visited the 10 venues. Photographs showing the highlights of the events are presented here.

3. Public awareness for school students

Bala Vidya Mandir Senior Secondary School, Adyar, Chennai, organised an inter school science exhibition on August 12, 2023, with the participation of IGCAR & MAPS, highlighting 'Atoms in the service of the Nation'.

Reported by
Smt. Jalaja Madan Mohan
Technical Coordination & Public Awareness Section
Safety, Quality & Resource Management Group

The 31st Prof. Brahm Prakash Memorial Materials Quiz (BPMMQ)

September 8-9, 2023

The 31st Prof. Brahm Prakash Memorial Materials Quiz (BPMMQ) was organized by the Indian Institute of Metals-Kalpakkam Chapter and the Indira Gandhi Centre for Atomic Research, in Kalpakkam during September 8-9, 2023, drawing participation of 80 students in classes XI and XII and 40 escorts, hailing from towns and cities across India. The two-day event comprised of (i) a visit to nuclear facilities of Kalpakkam (ii) Materials quiz events of preliminary, semifinal, and Grand finale (iii) elocution contest on selected essays on Materials related topics and (iv) Prof Brahm Prakash Memorial lecture delivered by Prof. B.S. Murty, Director, IIT Hyderabad, on the topic "The Immeasurable Joy of Research". Release of BPMMQ -2023 Digest

Prof.B.S. Murty,Director, Hyderabad delivering BPMMQ 2023 Lecture

Release of BPMMQ -2023 Digest

Virtual inaugural address by Dr. N Kailaiselvi, Director General, Council of Scientific & Industrial Research & Secretary, Department of Scientific and Industrial Research

The Third International Conference on Structural Integrity (ICONS 2023) was organized by IGCAR, during 23-25 Aug 2023 at Mamallapuram. The co-organizers include IIT Madras, Indian Society for Non-destructive Testing, Kalpakkam Chapter, Indian Institute of Metals, Kalpakkam Chapter and Indian Structural Integrity Society. About 250 professionals and research scholars from national labs, research institutes, academia, industry, and regulatory agencies participated in ICONS 2023 to deliberate on recent developments in assessing structural integrity of structures and operating equipments in nuclear, defense, aerospace, chemical and oil industries and identify areas for further research. The technical programme comprised of 3 plenary, 10 keynote, 21 invited lectures and 200 contributory papers. Oral and poster presentations at ICONS covered topics such as mechanical behavior of materials, fatigue and fracture mechanics, failure analysis, high strain rate loading, small specimen testing, regulatory aspects, structural health monitoring, reliability and structural integrity assessment, fitness for service and remnant life assessment, structural materials and weldment, steel and concrete structures etc. About 20 firms participated in the exhibition with display of products related to structural integrity paving way for fruitful interaction with the participants.

Dr. V. Karthik
High-temperature Materials Technology Division
Materials Development & Technology Group

Best Paper/Poster Award

- Shri. Mantosh Mandal secured the 'Best Poster Presentation' award at the 4th Heat Treatment and Surface Engineering (HTSE-2023) conference, held at Chennai on 28 -30 September 2023.

Bio-diversity @ DAE Campus, Kalpakkam

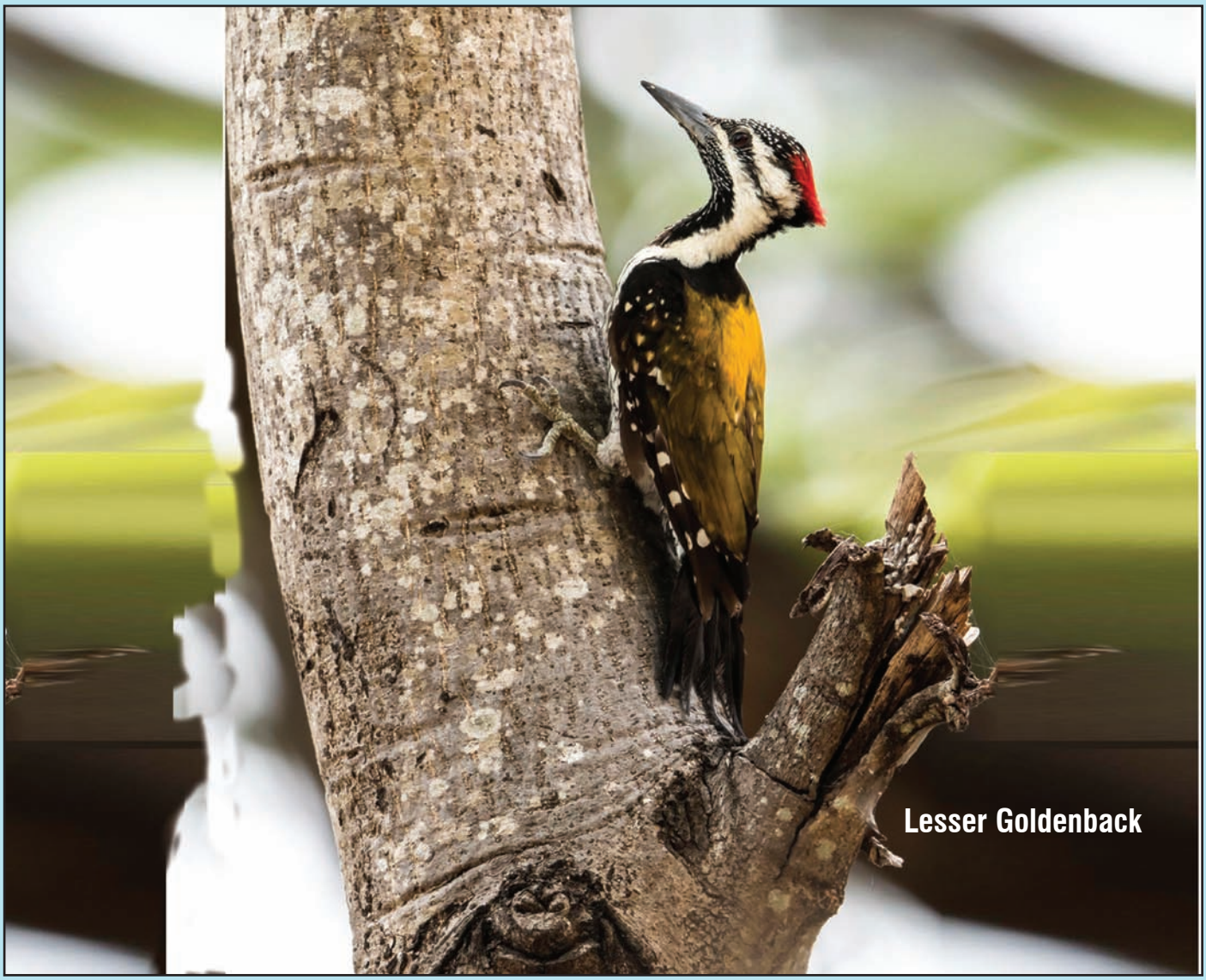

Lesser Goldenback are very common in both IGCAR campus and Kalpakkam township. It has a golden yellow and black upper plumage and black and white streaked lower parts and breast. Forehead differs in male and female, Female has a black forehead stippled with white and crimson hint crest. Mostly seen singly or in pairs

Published by Scientific Information Resource Division, SQ&RMG, IGCAR, Kalpakkam-603102